Physics   College of Arts and Sciences

9-15-2011

Implementation and Testing of the First Prompt Search for Electromagnetic Counterparts to Gravitational Wave Transients

Duncan Brown
Department of Physics, Syracuse University, Syracuse, NY

J. Abadie
California Institute of Technology

Stefan Ballmer
Syracuse University

Collin Capano
Syracuse University

P. Couvares
Syracuse University

Follow this and additional works at: https://surface.syr.edu/phy

Part of the Physics Commons

arXiv:1109.3498v1 [astro-ph.IM] 15 Sep 2011

Implementation and testing of the first prompt search for electromagnetic counterparts to gravitational wave transients

The LIGO Scientific Collaboration and Virgo Collaboration: J. Abadie[1], B. P. Abbott[1], R. Abbott[1], T. D. Abbott[2], M. Abernathy[3], T. Accadia[4], F. Acernese[5ac], C. Adams[6], R. Adhikari[1], C. Affeldt[7,8], P. Ajith[1], B. Allen[7,9,8], G. S. Allen[10], E. Amador Ceron[9], D. Amariutei[11], R. S. Amin[12], S. B. Anderson[1], W. G. Anderson[9], K. Arai[1], M. A. Arain[11], M. C. Araya[1], S. M. Aston[13], P. Astone[14a], D. Atkinson[15], P. Aufmuth[8,7], C. Aulbert[7,8], B. E. Aylott[13], S. Babak[16], P. Baker[17], G. Ballardin[18], S. Ballmer[19], D. Barker[15], F. Barone[5ac], B. Barr[3], P. Barriga[20], L. Barsotti[21], M. Barsuglia[22], M. A. Barton[15], I. Bartos[23], R. Bassiri[3], M. Bastarrika[3], A. Basti[24ab], J. Batch[15], J. Bauchrowitz[7,8], Th. S. Bauer[25a], M. Bebronne[4], B. Behnke[16], M.G. Beker[25a], A. S. Bell[3], A. Belletoile[4], I. Belopolski[23], M. Benacquista[26], J. M. Berliner[15], A. Bertolini[7,8], J. Betzwieser[1], N. Beveridge[3], P. T. Beyersdorf[27], I. A. Bilenko[28], G. Billingsley[1], J. Birch[6], R. Biswas[26], M. Bitossi[24a], M. A. Bizouard[29a], E. Black[1], J. K. Blackburn[1], L. Blackburn[30], D. Blair[20], B. Bland[15], M. Blom[25a], O. Bock[7,8], T. P. Bodiya[21], C. Bogan[7,8], R. Bondarescu[31], F. Bondu[32b], L. Bonelli[24ab], R. Bonnand[33], R. Bork[1], M. Born[7,8], V. Boschi[24a], S. Bose[34], L. Bosi[35a], B. Bouhou[22], S. Braccini[24a], C. Bradaschia[24a], P. R. Brady[9], V. B. Braginsky[28], M. Branchesi[36ab], J. E. Brau[37], J. Breyer[7,8], T. Briant[38], D. O. Bridges[6], A. Brillet[32a], M. Brinkmann[7,8], V. Brisson[29a], M. Britzger[7,8], A. F. Brooks[1], D. A. Brown[19], A. Brummit[39], T. Bulik[40bc], H. J. Bulten[25ab], A. Buonanno[41], J. Burguet–Castell[9], O. Burmeister[7,8], D. Buskulic[4], C. Buy[22], R. L. Byer[10], L. Cadonati[42], G. Cagnoli[36a], J. Cain[43], E. Calloni[5ab], J. B. Camp[30], P. Campsie[3], J. Cannizzo[30], K. Cannon[44], B. Canuel[18], J. Cao[45], C. D. Capano[19], F. Carbognani[18], S. Caride[46], S. Caudill[12], M. Cavaglià[43], F. Cavalier[29a], R. Cavalieri[18], G. Cella[24a], C. Cepeda[1], E. Cesarini[36b], O. Chaibi[32a], T. Chalermsongsak[1], E. Chalkley[13], P. Charlton[47], E. Chassande-Mottin[22], S. Chelkowski[13], Y. Chen[48], A. Chincarini[49], A. Chiummo[18], H. Cho[50], N. Christensen[51], S. S. Y. Chua[52], C. T. Y. Chung[53], S. Chung[20], G. Ciani[11], F. Clara[15], D. E. Clark[10], J. Clark[54], J. H. Clayton[9], F. Cleva[32a], E. Coccia[55ab], P-F. Cohadon[38], C. N. Colacino[24ab], J. Colas[18], A. Colla[14ab], M. Colombini[14b], A. Conte[14ab], R. Conte[56], D. Cook[15], T. R. Corbitt[21], M. Cordier[27], N. Cornish[17], A. Corsi[1], C. A. Costa[12], M. Coughlin[51], J.-P. Coulon[32a], P. Couvares[19], D. M. Coward[20], D. C. Coyne[1], J. D. E. Creighton[9], T. D. Creighton[26], A. M. Cruise[13], A. Cumming[3], L. Cunningham[3], E. Cuoco[18], R. M. Cutler[13], K. Dahl[7,8], S. L. Danilishin[28], R. Dannenberg[1], S. D'Antonio[55a], K. Danzmann[7,8], V. Dattilo[18], B. Daudert[1], H. Daveloza[26], M. Davier[29a], G. Davies[54], E. J. Daw[57], R. Day[18], T. Dayanga[34], R. De Rosa[5ab], D. DeBra[10], G. Debreczeni[58], J. Degallaix[7,8], W. Del Pozzo[25a], M. del Prete[59b], T. Dent[54], V. Dergachev[1], R. DeRosa[12], R. DeSalvo[1], V. Dhillon[57], S. Dhurandhar[60], L. Di Fiore[5a], A. Di Lieto[24ab], I. Di Palma[7,8], M. Di Paolo Emilio[55a], A. Di Virgilio[24a], M. Díaz[26], A. Dietz[4], F. Donovan[21], K. L. Dooley[11], S. Dorsher[61], M. Drago[59ab], R. W. P. Drever[62], J. C. Driggers[1], Z. Du[45], J.-C. Dumas[20], S. Dwyer[21], T. Eberle[7,8], M. Edgar[3], M. Edwards[54], A. Effler[12], P. Ehrens[1], G. Endrőczi[58], R. Engel[1], T. Etzel[1], K. Evans[3], M. Evans[21], T. Evans[6], M. Factourovich[23], V. Fafone[55ab], S. Fairhurst[54], Y. Fan[20], B. F. Farr[63], W. Farr[63], D. Fazi[63], H. Fehrmann[7,8], D. Feldbaum[11], I. Ferrante[24ab], F. Fidecaro[24ab], L. S. Finn[31], I. Fiori[18], R. P. Fisher[31], R. Flaminio[33], M. Flanigan[15], S. Foley[21], E. Forsi[6], L. A. Forte[5a], N. Fotopoulos[1], J.-D. Fournier[32a], J. Franc[33], S. Frasca[14ab], F. Frasconi[24a], M. Frede[7,8], M. Frei[64], Z. Frei[65], A. Freise[13], R. Frey[37], T. T. Fricke[12], J. K. Fridriksson[21], D. Friedrich[7,8], P. Fritschel[21], V. V. Frolov[6], P. J. Fulda[13], M. Fyffe[6], M. Galimberti[33], L. Gammaitoni[35ab], M. R. Ganija[66], J. Garcia[15], J. A. Garofoli[19], F. Garufi[5ab], M. E. Gáspár[58], G. Gemme[49], R. Geng[45], E. Genin[18], A. Gennai[24a], L. Á. Gergely[67], S. Ghosh[34], J. A. Giaime[12,6], S. Giampanis[9], K. D. Giardina[6], A. Giazotto[24a], C. Gill[3], E. Goetz[7,8], L. M. Goggin[9], G. González[12], M. L. Gorodetsky[28], S. Goßler[7,8], R. Gouaty[4], C. Graef[7,8], M. Granata[22], A. Grant[3], S. Gras[20], C. Gray[15], N. Gray[3], R. J. S. Greenhalgh[39], A. M. Gretarsson[68], C. Greverie[32a], R. Grosso[26], H. Grote[7,8], S. Grunewald[16], G. M. Guidi[36ab], C. Guido[6], R. Gupta[60], E. K. Gustafson[1], R. Gustafson[46], T. Ha[69], B. Hage[8,7], J. M. Hallam[13], D. Hammer[9], G. Hammond[3], J. Hanks[15], C. Hanna[1,70], J. Hanson[6], J. Harms[62], G. M. Harry[21], I. W. Harry[54], E. D. Harstad[37], M. T. Hartman[11], K. Haughian[3], K. Hayama[71], J.-F. Hayau[32b], T. Hayler[39], J. Heefner[1], A. Heidmann[38], M. C. Heintze[11], H. Heitmann[32], P. Hello[29a], M. A. Hendry[3], I. S. Heng[3], A. W. Heptonstall[1], V. Herrera[10], M. Hewitson[7,8], S. Hild[3], D. Hoak[42], K. A. Hodge[1], K. Holt[6], J. Homan[21], T. Hong[48], S. Hooper[20], D. J. Hosken[66], J. Hough[3], E. J. Howell[20], B. Hughey[9], S. Husa[72], S. H. Huttner[3], T. Huynh-Dinh[6], D. R. Ingram[15], R. Inta[52], T. Isogai[51], A. Ivanov[1], K. Izumi[71], M. Jacobson[1], H. Jang[73], P. Jaranowski[40d], W. W. Johnson[12], D. I. Jones[74], G. Jones[54], R. Jones[3], L. Ju[20], P. Kalmus[1], V. Kalogera[63], I. Kamaretsos[54], S. Kandhasamy[61], G. Kang[73], J. B. Kanner[41], E. Katsavounidis[21], W. Katzman[6], H. Kaufer[7,8], K. Kawabe[15], S. Kawamura[71], F. Kawazoe[7,8], W. Kells[1], D. G. Keppel[1], Z. Keresztes[67], A. Khalaidovski[7,8], F. Y. Khalili[28], E. A. Khazanov[75], B. Kim[73], C. Kim[76], D. Kim[20], H. Kim[7,8], K. Kim[77], N. Kim[10], Y.-M. Kim[50], P. J. King[1], M. Kinsey[31], D. L. Kinzel[6], J. S. Kissel[21], S. Klimenko[11], K. Kokeyama[13], V. Kondrashov[1], R. Kopparapu[31], S. Koranda[9], W. Z. Korth[1], I. Kowalska[40b], D. Kozak[1], V. Kringel[7,8], S. Krishnamurthy[63], B. Krishnan[16], A. Królak[40ae], G. Kuehn[7,8], R. Kumar[3], P. Kwee[8,7], M. Laas-Bourez[20], P. K. Lam[52], M. Landry[15], M. Lang[31], B. Lantz[10], N. Lastzka[7,8], C. Lawrie[3], A. Lazzarini[1], P. Leaci[16], C. H. Lee[50], H. M. Lee[78], N. Leindecker[10], J. R. Leong[7,8], I. Leonor[37], N. Leroy[29a], N. Letendre[4], J. Li[45], T. G. F. Li[25a], N. Liguori[59ab], P. E. Lindquist[1], N. A. Lockerbie[79], D. Lodhia[13], M. Lorenzini[36a], V. Loriette[29b], M. Lormand[6], G. Losurdo[36a], J. Luan[48], M. Lubinski[15], H. Lück[7,8], A. P. Lundgren[31], E. Macdonald[3], B. Machenschalk[7,8], M. MacInnis[21], D. M. Macleod[54], M. Mageswaran[1], K. Mailand[1], E. Majorana[14a], I. Maksimovic[29b], N. Man[32a], I. Mandel[21], V. Mandic[61], M. Mantovani[24ac], A. Marandi[10], F. Marchesoni[35a], F. Marion[4], S. Márka[23], Z. Márka[23], A. Markosyan[10], E. Maros[1], J. Marque[18], F. Martelli[36ab], I. W. Martin[3], R. M. Martin[11], J. N. Marx[1], K. Mason[21], A. Masserot[4], F. Matichard[21], L. Matone[23], R. A. Matzner[64], N. Mavalvala[21], G. Mazzolo[7,8], R. McCarthy[15], D. E. McClelland[52], P. McDaniel[21], S. C. McGuire[80], G. McIntyre[1], D. J. A. McKechan[54], G. D. Meadors[46], M. Mehmet[7,8], T. Meier[8,7], A. Melatos[53], A. C. Melissinos[81], G. Mendell[15], D. Menendez[31], R. A. Mercer[9], L. Merill[20], S. Meshkov[1], C. Messenger[54], M. S. Meyer[6], H. Miao[20], C. Michel[33], L. Milano[5ab], J. Miller[52], Y. Minenkov[55a], V. P. Mitrofanov[28], G. Mitselmakher[11], R. Mittleman[21], O. Miyakawa[71], B. Moe[9], P. Moesta[16], M. Mohan[18], S. D. Mohanty[26], S. R. P. Mohapatra[42], D. Moraru[15], G. Moreno[15], N. Morgado[33], A. Morgia[55ab], T. Mori[71], S. Mosca[5ab], K. Mossavi[7,8], B. Mours[4], C. M. Mow–Lowry[52], C. L. Mueller[11], G. Mueller[11], S. Mukherjee[26], A. Mullavey[52], H. Müller-Ebhardt[7,8], J. Munch[66], P. G. Murray[3], A. Mytidis[11], T. Nash[1], L. Naticchioni[14ab], R. Nawrodt[3], V. Necula[11], J. Nelson[3], G. Newton[3], E. Nishida[71], A. Nishizawa[71], F. Nocera[18], D. Nolting[6], L. Nuttall[54], E. Ochsner[41], J. O'Dell[39], E. Oelker[21], G. H. Ogin[1], J. J. Oh[69], S. H. Oh[69], R. G. Oldenburg[9], B. O'Reilly[6], R. O'Shaughnessy[9], C. Osthelder[1], C. D. Ott[48], D. J. Ottaway[66], R. S. Ottens[11], H. Overmier[6], B. J. Owen[31], A. Page[13], G. Pagliaroli[55ac], L. Palladino[55ac], C. Palomba[14a], Y. Pan[41], C. Pankow[11], F. Paoletti[24a,18], M. A. Papa[16,9], M. Parisi[5ab], A. Pasqualetti[18], R. Passaquieti[24ab], D. Passuello[24a], P. Patel[1], D. Pathak[54], M. Pedraza[1], P. Peiris[82], L. Pekowsky[19], S. Penn[83], C. Peralta[16], A. Perreca[19], G. Persichetti[5ab], M. Phelps[1], M. Pickenpack[7,8], F. Piergiovanni[36ab], M. Pietka[40d], L. Pinard[33], I. M. Pinto[84], M. Pitkin[3], H. J. Pletsch[7,8], M. V. Plissi[3], R. Poggiani[24ab], J. Pöld[7,8], F. Postiglione[56], M. Prato[49], V. Predoi[54], L. R. Price[1], M. Prijatelj[7,8], M. Principe[84], S. Privitera[1], R. Prix[7,8], G. A. Prodi[59ab], L. Prokhorov[28], O. Puncken[7,8], M. Punturo[35a], P. Puppo[14a], V. Quetschke[26], F. J. Raab[15], D. S. Rabeling[25ab], I. Rácz[58], H. Radkins[15], P. Raffai[65], M. Rakhmanov[26], C. R. Ramet[6], B. Rankins[43], P. Rapagnani[14ab], S. Rapoport[52,92], V. Raymond[63], V. Re[55ab], K. Redwine[23], C. M. Reed[15], T. Reed[85], T. Regimbau[32a], S. Reid[3], D. H. Reitze[11], F. Ricci[14ab], R. Riesen[6], K. Riles[46], N. A. Robertson[1,3], F. Robinet[29a], C. Robinson[54], E. L. Robinson[16], A. Rocchi[55a], S. Roddy[6], C. Rodriguez[63], M. Rodruck[15], L. Rolland[4], J. Rollins[23], J. D. Romano[26], R. Romano[5ac], J. H. Romie[6], D. Rosińska[40cf], C. Röver[7,8], S. Rowan[3], A. Rüdiger[7,8], P. Ruggi[18], K. Ryan[15], H. Ryll[7,8], P. Sainathan[11], M. Sakosky[15], F. Salemi[7,8], L. Sammut[53], L. Sancho de la Jordana[72], V. Sandberg[15], S. Sankar[21], V. Sannibale[1], L. Santamaría[1], I. Santiago-Prieto[3], G. Santostasi[86], B. Sassolas[33], B. S. Sathyaprakash[54], S. Sato[71], M. Satterthwaite[52], P. R. Saulson[19], R. L. Savage[15], R. Schilling[7,8], S. Schlamminger[87], R. Schnabel[7,8], R. M. S. Schofield[37], B. Schulz[7,8], B. F. Schutz[16,54], P. Schwinberg[15], J. Scott[3], S. M. Scott[52], A. C. Searle[1], F. Seifert[1], D. Sellers[6], A. S. Sengupta[1], D. Sentenac[18], A. Sergeev[75], D. A. Shaddock[52], M. Shaltev[7,8], B. Shapiro[21], P. Shawhan[41], D. H. Shoemaker[21], A. Sibley[6], X. Siemens[9], D. Sigg[15], A. Singer[1], L. Singer[1], A. M. Sintes[72], G. Skelton[9], B. J. J. Slagmolen[52], J. Slutsky[12], J. R. Smith[2], M. R. Smith[1], N. D. Smith[21], R. J. E. Smith[13], K. Somiya[48], B. Sorazu[3], J. Soto[21], F. C. Speirits[3], L. Sperandio[55ab], A. J. Stein[21], E. Steinert[15], J. Steinlechner[7,8], S. Steinlechner[7,8], S. Steplewski[34], A. Stochino[1], R. Stone[26], K. A. Strain[3], S. Strigin[28], A. S. Stroeer[26], R. Sturani[36ab], A. L. Stuver[6], T. Z. Summerscales[88], M. Sung[12], S. Susmithan[20], P. J. Sutton[54], B. Swinkels[18], M. Tacca[18], L. Taffarello[59c], D. Talukder[34], D. B. Tanner[11], S. P. Tarabrin[7,8], J. R. Taylor[7,8], R. Taylor[1], P. Thomas[15], K. A. Thorne[6], K. S. Thorne[48], E. Thrane[61], A. Thüring[8,7], C. Titsler[31], K. V. Tokmakov[79], A. Toncelli[24ab], M. Tonelli[24ab], O. Torre[24ac], C. Torres[6], C. I. Torrie[1,3], E. Tournefier[4], F. Travasso[35ab], G. Traylor[6], M. Trias[72], K. Tseng[10], L. Turner[1], D. Ugolini[89], K. Urbanek[10], H. Vahlbruch[8,7], G. Vajente[24ab], M. Vallisneri[48], J. F. J. van den Brand[25ab], C. Van Den Broeck[25a], S. van der Putten[25a], A. A. van Veggel[3], S. Vass[1], M. Vasuth[58], R. Vaulin[21], M. Vavoulidis[29a], A. Vecchio[13], G. Vedovato[59c], J. Veitch[54], P. J. Veitch[66], C. Veltkamp[7,8], D. Verkindt[4], F. Vetrano[36ab], A. Viceré[36ab], A. E. Villar[1], J.-Y. Vinet[32a], S. Vitale[68], S. Vitale[25a], H. Vocca[35a], C. Vorvick[15], S. P. Vyatchanin[28], A. Wade[52], S. J. Waldman[21], L. Wallace[1], Y. Wan[45], X. Wang[45], Z. Wang[45], A. Wanner[7,8], R. L. Ward[22], M. Was[29a], P. Wei[19], M. Weinert[7,8], A. J. Weinstein[1], R. Weiss[21], L. Wen[48,20], S. Wen[6], P. Wessels[7,8], M. West[19], T. Westphal[7,8], K. Wette[7,8], J. T. Whelan[82], S. E. Whitcomb[1,20], D. White[57], B. F. Whiting[11], C. Wilkinson[15], P. A. Willems[1], H. R. Williams[31], L. Williams[11], B. Willke[7,8], L. Winkelmann[7,8], W. Winkler[7,8], C. C. Wipf[21], A. G. Wiseman[9], H. Wittel[7,8], G. Woan[3], R. Wooley[6], J. Worden[15], J. Yablon[63], I. Yakushin[6], H. Yamamoto[1], K. Yamamoto[7,8], H. Yang[48], D. Yeaton-Massey[1], S. Yoshida[90], P. Yu[9], M. Yvert[4], A. Zadrożny[40e,91], M. Zanolin[68], J.-P. Zendri[59c], F. Zhang[45], L. Zhang[1], W. Zhang[45], Z. Zhang[20], C. Zhao[20], N. Zotov[85], M. E. Zucker[21], J. Zweizig[1],

M. Boer[93], R. Fender[74], N. Gehrels[30], A. Klotz[94], E. O. Ofek[62,95], M. Smith[31], M. Sokolowski[91], B. W. Stappers[96], I. Steele[97], J. Swinbank[98], and R. A. M. J. Wijers[98]

(Affiliations can be found after the references)

ABSTRACT

Aims. A transient astrophysical event observed in both gravitational wave (GW) and electromagnetic (EM) channels would yield rich scientific rewards. A first program initiating EM follow-ups to possible transient GW events has been developed and exercised by the LIGO and Virgo community in association with several partners. In this paper, we describe and evaluate the methods used to promptly identify and localize GW event candidates and to request images of targeted sky locations.

Methods. During two observing periods (Dec 17 2009 to Jan 8 2010 and Sep 2 to Oct 20 2010), a low-latency analysis pipeline was used to identify GW event candidates and to reconstruct maps of possible sky locations. A catalog of nearby galaxies and Milky Way globular clusters was used to select the most promising sky positions to be imaged, and this directional information was delivered to EM observatories with time lags of about thirty minutes. A Monte Carlo simulation has been used to evaluate the low-latency GW pipeline's ability to reconstruct source positions correctly.

Results. For signals near the detection threshold, our low-latency algorithms often localized simulated GW burst signals to tens of square degrees, while neutron star/neutron star inspirals and neutron star/black hole inspirals were localized to a few hundred square degrees. Localization precision improves for moderately stronger signals. The correct sky location of signals well above threshold and originating from nearby galaxies may be observed with ~50% or better probability with a few pointings of wide-field telescopes.

Key words. gravitational waves - methods: observational

1. Introduction

The Laser Interferometer Gravitational-Wave Observatory (LIGO) (Abbott et al. 2009a) and Virgo (Accadia et al. 2011) have taken significant steps toward gravitational wave (GW) astronomy over the past decade. The LIGO Scientific Collaboration operates two LIGO observatories in the U.S. along with the GEO 600 detector (Lück et al. 2010) in Germany. Together with Virgo, located in Italy, they form a detector network capable of detecting GW signals arriving from all directions. Their most recent joint data taking run was between July 2009 and October 2010. GEO 600 and Virgo are currently operating during summer 2011, while the LIGO interferometers have been decommissioned for the upgrade to the next-generation Advanced LIGO detectors (Harry et al. 2010), expected to be operational around 2015. Virgo will also be upgraded to become Advanced Virgo (Acernese et al. 2008). Additionally, the new LCGT detector (Kuroda & The LCGT Collaboration 2010) is planned in Japan. These "advanced era" detectors are expected to detect compact binary coalescences, possibly at a rate of dozens per year, after reaching design sensitivity (Abadie et al. 2010b).

Detectable, transient GW signals in the LIGO/Virgo frequency band require bulk motion of mass on short time scales. Emission in other channels is also possible in many such rapidly changing massive systems. This leads to the prospect that some transient GW sources may have corresponding electromagnetic (EM) counterparts which could be discovered with a low latency response to GW triggers (Sylvestre 2003; Kanner et al. 2008; Stubbs 2008; Kulkarni & Kasliwal 2009; Bloom et al. 2009).

Finding these EM counterparts would yield rich scientific rewards (see Sect. 2), but is technically challenging due to imperfect localization of the gravitational wave signal and uncertainty regarding the relative timing of the GW and EM emissions. This paper details our recent effort to construct a prompt search for joint GW/EM sources between the LIGO/Virgo detector network and partner EM observatories (see Sect. 3). The search was demonstrated during two periods of live LIGO/Virgo running: the "winter" observing period in December 2009 and January 2010 and the "autumn" observing period in September and October 2010. We focus here on the design and performance of software developed for rapid EM follow-ups of GW candidate events, as well as the procedures used to identify significant GW triggers and to communicate the most likely sky locations to partner EM observatories. The analysis of the observational data is in progress, and will be the subject of future publications.

2. Motivation

2.1. Sources

A variety of EM emission mechanisms, both observed and theoretical, may occur in association with observable GW sources. Characteristics of a few scenarios helped inform the design and execution of this search. Here, some likely models are presented, along with characteristics of the associated EM emission.

2.1.1. Compact Binary Coalescence

Compact binary systems consisting of neutron stars and/or black holes are thought to be the most common sources of GW emission detectable with ground-based interferometers. Radiation of energy and angular momentum causes the orbit to decay (inspiral) until the objects merge (Cutler et al. 1993). For a system consisting of two neutron stars (NS-NS) or a neutron star and a stellar-mass black hole (NS-BH), the inspiral stage produces the most readily detectable GW signal. The energy flux reaching Earth depends on the inclination angle of the binary orbit relative to the line of sight. The initial LIGO-Virgo network is sensitive to optimally oriented NS-NS mergers from as far away as 30 Mpc, and mergers between a NS and a $10\,M_\odot$ black hole out to 70 Mpc (Abadie et al. 2010b). With advanced detectors, these range limits are expected to increase to 440 and 930 Mpc, respectively.

The energetics of these systems suggest that an EM counterpart is also likely. The final plunge radiates of order 10^{53} ergs of gravitational binding energy as gravitational waves. If even a small fraction of this energy escapes as photons in the observing band, the resulting counterpart could be observable to large distances. The EM transients that are likely to follow a NS-BH or NS-NS merger are described below.

Short-hard gamma-ray bursts (SGRBs), which typically have durations of 2 seconds or less, may be powered by NS-NS or NS-BH mergers (Nakar 2007; Mészáros 2006; Piran 2004). Afterglows of SGRBs have been observed in wavelengths from radio to X-ray, and out to Gpc distances (Nakar 2007; Gehrels et al. 2009). Optical afterglows have been observed from a few tens of seconds to a few days after the GRB trigger (see, for example, Klotz et al. (2009a)), and fade with a power law $t^{-\alpha}$, where α is between 1 and 1.5. At 1 day after the trigger time, the apparent optical magnitude would be between 12 and 20 for a source at 50 Mpc (Kann et al. 2011), comparable to the distance to which LIGO and Virgo could detect the merger.

Even if a compact binary coalescence is not observable in gamma-rays, there is reason to expect it will produce an observable optical counterpart. Li & Paczyński (1998) suggested that, during a NS-NS or NS-BH merger, some of the neutron star's mass is tidally ejected. In their model, the ejected neutron-rich matter produces heavy elements through r-process nucleosynthesis, which subsequently decay and heat the ejecta, powering an optical afterglow known as a kilonova. The predicted optical emission is roughly isotropic, and so is observable regardless of the orientation of the original binary system. This emission is expected to peak after about one day, around magnitude 18 for a source at 50 Mpc (Metzger et al. 2010), and then fade over the course of a few days following the merger.

2.1.2. Stellar Core Collapse

Beyond the compact object mergers described above, some other astrophysical processes are plausible sources of observable GW emission. GW transients with unknown waveforms may be discovered by searching the LIGO and Virgo data for short periods of excess power (bursts). The EM counterparts to some likely sources of GW burst signals are described below.

Core-collapse supernovae are likely to produce some amount of gravitational radiation, though large uncertainties still exist in the expected waveforms and energetics. Most models predict GW spectra that would be observable by initial LIGO and Virgo from distances within some fraction of the Milky Way, but not from the Mpc distances needed to observe GWs from another galaxy (Ott 2009). Neutrino detectors such as SuperKamiokande and IceCube should also detect a large number of neutrinos from a Galactic supernova (Beacom & Vogel 1999; Halzen & Raffelt 2009; Leonor et al. 2010). Galactic supernovae normally would be very bright in the optical band, but could be less than obvious if obscured by dust or behind the Galactic center. Optical emission would first appear hours after the GW and neutrino signal

and would peak days to weeks later, fading over the course of weeks or months.

Long-soft gamma-ray bursts (LGRBs) are believed to be associated with the core collapse of massive stars (Woosley 1993; MacFadyen & Woosley 1999; Piran 2004; Woosley & Bloom 2006; Metzger et al. 2011). A large variety of possible GW emitting mechanisms within these systems have been proposed, with some models predicting GW spectra that would be observable from distances of a few Mpc with initial LIGO and Virgo (Fryer et al. 2002; Kobayashi & Mészáros 2003a; Corsi & Mészáros 2009; Piro & Pfahl 2007; Korobkin et al. 2011; Kiuchi et al. 2011). The afterglows of LGRBs, like the afterglows of SGRBs, typically show power law fading with $\alpha = 1 - 1.5$. However, the peak isotropic equivalent luminosity of LGRB afterglows is typically a factor of 10 brighter than SGRB afterglows (Nakar 2007; Kann et al. 2010).

An off-axis or sub-energetic LGRB may also be observed as an orphan afterglow or dirty fireball (Granot et al. 2002; Rhoads 2003). These transients brighten over the course of several days or even weeks, depending on the observing band and viewing angle. Identifying orphan afterglows in large area surveys, such as Rykoff et al. (2005), has proven difficult, but a GW trigger may help distinguish orphan afterglows from other EM variability.

2.1.3. Other Possible Sources

Cosmic string cusps are another possible joint source of GW (Siemens et al. 2006; Damour & Vilenkin 2000) and EM (Vachaspati 2008) radiation. If present, their distinct GW signature will distinguish them from other sources. On the other hand, even unmodeled GW emissions can be detected using GW burst search algorithms, and such events may in some cases produce EM radiation either through internal dynamics or through interaction with the surrounding medium. Thus, our joint search methods should allow for a wide range of possible sources.

2.2. Investigations enabled by joint GW/EM observations

A variety of astrophysical information could potentially be extracted from a joint GW/EM signal. In understanding the progenitor physics, the EM and GW signals are essentially complementary. The GW time series directly traces the bulk motion of mass in the source, whereas EM emissions arising from outflows or their interaction with the interstellar medium give only indirect information requiring inference and modeling. On the other hand, observing an EM counterpart to a GW signal reduces the uncertainty in the source position from degrees to arcseconds. This precise directional information can lead to identification of a host galaxy, and a measurement of redshift. Some specific questions that may be addressed with a collection of joint GW/EM signals are discussed below.

If the GW source is identified as a NS-NS or NS-BH merger, additional investigations are enabled with an EM counterpart. The observation of the EM signal will improve the estimation of astrophysical source parameters. For example, when attempting parameter estimation with a bank of templates and a single data stream, the source's distance, inclination angle, and angular position are largely degenerate. A precise source position from an EM counterpart would help break this degeneracy (Dalal et al. 2006; Nissanke et al. 2010). High precision parameter estimation may even constrain the NS equation of state (Cutler et al. 1993; Vallisneri 2000; Flanagan & Hinderer 2008;

Andersson et al. 2011; Pannarale et al. 2011; Hinderer et al. 2010).

Observing EM counterparts of NS-NS and NS-BH merger events will give strong evidence as to which class of source, if either, is the source of SGRBs (Bloom et al. 2009). In addition, if some neutron star mergers are the sources of SGRBs, a collection of joint EM/GW observations would allow an estimate of the SGRB jet opening angle by comparing the number of merger events with and without observable prompt EM emission, and some information would be obtainable even from a single loud event (Kobayashi & Mészáros 2003b; Seto 2007).

An ensemble of these observations could provide a novel measurement of cosmological parameters. Analysis of the well-modeled GW signal will provide a measurement of the luminosity distance to the source, while the redshift distance is measurable from the EM data. Taken together, they provide a direct measurement of the local Hubble constant (Schutz 1986; Markovic 1993; Dalal et al. 2006; Nissanke et al. 2010).

Finally, all of the above assume that general relativity is the correct theory of gravity on macroscopic scales. Joint EM/GW observations can also be used to test certain predictions of general relativity, such as the propagation speed and polarizations of GWs. (Will 2005; Yunes et al. 2010; Kahya 2011).

In the case that the transient GW source is not a binary merger event, the combination of GW and EM information will again prove very valuable. In this scenario, the gravitational waveform will not be known a priori. Any distance estimate would be derived from the EM data, which would then set the overall scale for the energy released as GWs.

As in the merger case, the linking of a GW signal with a known EM phenomenon will provide insight into the underlying physical process. For example, the details of the central engine that drives LGRBs are unknown. The GW signal could give crucial clues to the motion of matter in the source, and potentially distinguish between competing models. A similar insight into the source mechanism could be achieved for an observation of GW emission associated with a supernova. Rapid identification may also allow observation of a supernova in its earliest moments, an opportunity that currently depends on luck (Soderberg et al. 2008).

2.3. Extend GW Detector Reach

Finding an EM counterpart associated with a LIGO/Virgo trigger would increase confidence that a truly astrophysical event had been observed in the GW data. Using EM transients to help distinguish low amplitude GW signals from noise events allows a lowering of the detection threshold, as was done in searches such as Abbott et al. (2010). Kochanek & Piran (1993) estimated that the detectable amplitude could be reduced by as much as a factor of 1.5, increasing the effective detector horizon distance (the maximum distance at which an optimally oriented and located system could be detected) by the same factor and thus increasing the detection rate by a factor of 3. In practice, the actual improvement in GW sensitivity achieved by pairing EM and GW observations depends on many factors unique to each search, including details of the source model and data set, and so is difficult to predict in advance.

In the case of a coincidence between a GW signal and a discovered EM transient, the joint significance may be calculated by assuming that the backgrounds of the EM and GW search are independent. The False Alarm Rate (FAR) of a GW/EM coincidence is the FAR of the GW signal, as described in Sect. 4.2, times α, the expected fraction of observations associated with a

false or unrelated EM transient. The false alarm fraction α may be estimated using fields from surveys not associated with GW triggers. The value of α will depend heavily on the telescope being used, the cuts selected in image analysis, galactic latitude of the source and other factors.

To use EM transience in this way, the time-domain sky in the wavelength of interest must be well understood. Transients that are found in directional and time coincidence with GW triggers would increase confidence in the GW signal only if the chance of a similar, incidental coincidence is understood to be low (Kulkarni & Kasliwal 2009).

2.4. Implications for Search Design

Characteristics of the target sources helped determine when and where to seek the EM counterparts to GW event candidates. For reasons discussed in this section, the search strategy presented in this paper emphasizes capturing images as soon as possible after the GW trigger, along with follow-up images over subsequent nights. Some of the most probable models are extragalactic, and so field selection was strongly weighted towards regions containing nearby galaxies.

The observations and theoretical models of EM transients discussed above provided guidance when choosing the observing cadence. GRB optical afterglows have been observed during the prompt emission phase (Klotz et al. 2009b) and up to many hours after the trigger. For this search, the first attempt to image the source position was made as soon as possible after validating a GW trigger. In both the kilonova (Li & Paczyński 1998) and supernova (Ott 2009) models, some time lag exists between the release of GW and EM emission, primarily due to the time it takes the outflowing material to become optically thin. This time lag may be from several hours for a kilonova, up to days for a core-collapse supernova. Furthermore, Coward et al. (2011) show that for GRBs that are off-axis, the optical afterglow may not be visible until days after the burst. For these reasons, repeated observations over several nights are desirable. Also, the light curves obtained by observing the same fields over multiple nights are critical clues for discovering and classifying transient sources.

Knowing where to look for the counterpart to a GW trigger is challenging. Directional estimates of low signal to noise ratio (SNR) binary inspiral sources with the 2009–10 GW detector network have uncertainties of several tens of square degrees (Fairhurst 2009). This suggests using telescopes with a field of view (FOV) of at least a few square degrees if possible. Even with such a "wide field" instrument, there is a striking mismatch between the large area needing to be searched, and the size of a single FOV.

The problem may be partially mitigated by making use of the known mass distribution in the nearby universe. A search for GW counterparts can dramatically reduce the needed sky coverage by focusing observations on galaxies within the distance limits of the GW detectors (Kanner et al. 2008; Nuttall & Sutton 2010). Limiting the search area to known galaxies may also improve the feasibility of identifying the true counterpart from among other objects with time-varying EM emissions (Kulkarni & Kasliwal 2009). Even within the Milky Way, a search may emphasize known targets by seeking counterparts within globular clusters, where binary systems of compact objects may form efficiently (O'Leary et al. 2007).

An emphasis on extragalactic and globular-cluster sources has the potential drawback that any counterparts in the plane of the Milky Way may be missed. Also, neutron star mergers that occur at large distances from their host galaxies may not be observed, though the population with large kicks should be small (Berger 2010; Kelley et al. 2010).

Our selection of fields to observe was weighted towards areas containing known galaxies within 50 Mpc. The utilized catalog of nearby galaxies and globular clusters, and the process for selecting fields to observe, is described in Sect. 5.

3. GW and EM Instruments

3.1. Gravitational Wave Detector Network

The LIGO and Virgo detectors are based on Michelson-type interferometers, with Fabry-Perot cavities in each arm and a power recycling mirror between the laser and beamsplitter to dramatically increase the power in the arms relative to a simple Michelson design. The GEO 600 detector uses a folded interferometer without Fabry-Perot arm cavities but with an additional recycling mirror at the output to resonantly enhance the GW signal. As a gravitational wave passes through each interferometer, it induces a "strain" (a minuscule change in length on the order of 1 part in 10^{21} or less) on each arm of the interferometer due to the quadrupolar perturbation of the spacetime metric. The interferometers are designed to measure the *differential* strain on the two arms through interference of the laser light when the two beams are recombined at the beam splitter, with the relative optical phase modulated by the passing gravitational wave (Abbott et al. 2009a).

In 2009–2010 there were two operating LIGO interferometers, each with 4-km arms: H1, located near Hanford, Washington, and L1, located in Livingston Parish, Louisiana.[1] Virgo (V1) has arms of length 3 km and is located near Cascina, Italy. GEO 600 data was not used in the online search described in this paper, but was available for offline reanalysis of promising event candidates. The large physical separation between the instruments means that the effects of local environmental background can be mitigated by requiring a coincident signal in multiple interferometers. Each interferometer is most sensitive to GW signals traveling parallel or anti-parallel to zenith, but the antenna pattern varies gradually over the sky, so that the detectors are essentially all-sky monitors.

The EM follow-up program described in this paper was exercised during the 2009–2010 science runs. While single-detector triggers had been generated with low latency in earlier science runs for diagnostic and prototyping purposes, 2009–2010 was the first time that a systematic search for GW transients using the full LIGO-Virgo network was performed with low latency, and the first time that alerts were sent to external observatories.

3.2. Optical and Other Electromagnetic Observatories

In an effort to explore various approaches, the telescope network used in 2009–10 was intentionally heterogeneous. However, most of instruments had large fields of view to accommodate the imprecise GW position estimate. The approximate location of each EM observatory in shown in Fig. 1.

---

[1] Earlier science runs included a second interferometer at Hanford, called H2, with 2-km arms. H2 will reappear as part of Advanced LIGO, either as a second 4-km interferometer at Hanford or else at a site in Western Australia. The latter option would greatly improve the source localization capabilities of the network (Fairhurst 2011; Schutz 2011).

3.2.1. Optical Instruments

The *Palomar Transient Factory* (PTF) (Law et al. 2009; Rau et al. 2009) operates a 7.3 square degree FOV camera mounted on the 1.2 m Oschin Telescope at Palomar Observatory. A typical 60 s exposure detects objects with a limiting magnitude $R = 20.5$. For the autumn observing period, the PTF team devoted ten fields over several nights at a target rate of 1 trigger for every three weeks.

Pi of the Sky (Malek et al. 2009) observed using a camera with a 400 square degree FOV and exposures to limiting magnitude 11–12. It was located in Koczargi Stare, near Warsaw. The camera was a prototype for a planned system that will simultaneously image two steradians of sky. The target rate was approximately 1 per week in the autumn run, followed up with hundreds of 10 s exposures over several nights.

The *QUEST* camera (Baltay et al. 2007), currently mounted on the 1 m ESO Schmidt Telescope at La Silla Observatory, views 9.4 square degrees of sky in each exposure. The telescope is capable of viewing to a limiting magnitude of $R \sim 20$. The QUEST team devoted twelve 60 s exposures over several nights for each trigger in both the winter and autumn periods, with a target rate of 1 trigger per week.

ROTSE III (Akerlof et al. 2003) is a collection of four robotic telescopes spread around the world, each with a 0.45 m aperture and 3.4 square degree FOV. No filters are used, so the spectral response is that of the CCDs, spanning roughly 400 to 900 nm. The equivalent R band limiting magnitude is about 17 in a 20 s exposure. The ROTSE team arranged for a series of thirty images for the first night, and several images on following nights, for each autumn run trigger, with a target rate of 1 trigger per week.

SkyMapper (Keller et al. 2007) is a survey telescope located at Siding Spring observatory in Australia. The mosaic camera covers 5.7 square degrees of sky in each field, and is mounted on a 1.35 m telescope with a collecting area equivalent to an unobscured 1.01 m aperture. It is designed to reach a limiting magnitude $g \sim 21$ (>7 sigma) in a 110 s exposure. SkyMapper accepted triggers in the autumn run with a target rate of 1 per week, with several fields collected for each trigger.

TAROT (Klotz et al. 2009a) operates two robotic 25 cm telescopes, one at La Silla in Chile and one in Calern, France. Like the ROTSE III system, each TAROT instrument has a 3.4 square degree FOV. A 180 second image with TAROT in ideal conditions has a limiting R magnitude of 17.5. During the winter run, TAROT observed a single field during one night for each trigger. In the autumn run, the field selected for each trigger was observed over several nights. TAROT accepted triggers with a target rate of 1 per week.

Zadko Telescope (Coward et al. 2010) is a 1 m telescope located in Western Australia. The current CCD imager observes fields of 0.15 square degrees down to magnitude ~ 20 in the R band for a typical 180 s exposure. For each accepted trigger in the autumn run, Zadko repeatedly observed the five galaxies considered most likely to host the source over several nights. The target trigger rate for Zadko was one trigger per week.

The *Liverpool telescope* (Steele et al. 2004) is a 2 m robotic telescope situated at the Observatorio del Roque de Los Muchachos on La Palma. For this project the RATCam instrument, with a 21 square arcminute field of view, was used. This instrumentation allows a five minute exposure to reach magnitude $r' = 21$. This project was awarded 8 hours of target-of-opportunity time, which was split into 8 observations of 1 hour each, with a target rate of 1 trigger per week.
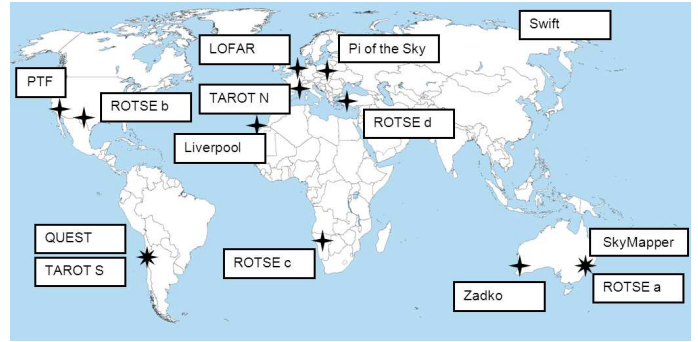

Fig. 1. A map showing the approximate positions of telescopes that participated in the project. The Swift satellite observatory is noted at an arbitrary location. The image is adapted from a blank world map placed in the public domain by P. Dlouhý.

3.2.2. Radio and X-ray Instruments

LOFAR (Fender et al. 2006; de Vos et al. 2009; Stappers et al. 2011) is a dipole array radio telescope based in the Netherlands but with stations across Europe. The array is sensitive to frequencies in the range of 30 to 80 MHz and 110 to 240 MHz, and can observe multiple simultaneous beams, each with a FWHM varying with frequency up to a maximum of around 23°. During the autumn run, LOFAR accepted triggers at a target rate of 1 per week and followed up each with a four-hour observation in its higher frequency band, providing a ~25 square degree field of view.

Although not used in the prompt search during the science run, the Expanded Very Large Array (Perley et al. 2011) was used to follow up a few triggers after the run with latencies of 3 and 5 weeks.

The *Swift* satellite (Gehrels et al. 2004) carries three instruments, each in different bands. Swift granted several target of opportunity observations with two of these, the X-ray Telescope (XRT) and UV/Optical Telescope (UVOT), for the winter and autumn observing periods. The XRT is an imaging instrument with a 0.15 square degree FOV, sensitive to fluxes around 10^{-13} ergs/cm^2/s in the 0.5-10 keV band. A few fields were imaged for each trigger that Swift accepted.

4. Trigger Selection

The online analysis process which produced GW candidate triggers to be sent to telescopes is outlined in Fig. 2. After data and information on data quality were copied from the interferometer sites to computing centers, three different data analysis algorithms identified triggers and determined probability skymaps. The process of downselecting this large collection of triggers to the few event candidates that received EM follow-up is described in this section.

After event candidates were placed in a central archive, additional software used the locations of nearby galaxies and Milky Way globular clusters to select likely source positions (Sect. 5). Triggers were manually vetted, then the selected targets were passed to partner observatories which imaged the sky in an attempt to find an associated EM transient. Studies demonstrating the performance of this pipeline on simulated GWs are presented in Sect. 6.
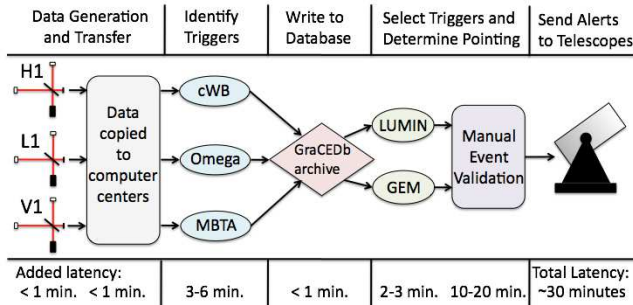
Fig. 2. A simplified flowchart of the online analysis with approximate time requirements for each stage. Data and information on data quality were generated at the Hanford, Livingston, and Virgo interferometers (H1, L1, and V1) and copied to centralized computer centers. The online event trigger generators produced coincident triggers which were written into the GraCEDb archive. The LUMIN and GEM algorithms selected statistically significant triggers from the archive and chose pointing locations. Significant triggers generated alerts, and were validated manually. If no obvious problem was found, the trigger's estimated coordinates were sent to telescopes for potential follow-up.

4.1. Trigger Generation

Sending GW triggers to observatories with less than an hour latency represents a major shift from past LIGO/Virgo data analyses, which were reported outside the collaboration at soonest several months after the data collection. Reconstructing source positions requires combining the data streams from the LIGO-Virgo network using either fully coherent analysis or a coincidence analysis of single-detector trigger times. A key step in latency reduction was the rapid data replication process, in which data from all three GW observatory sites were copied to several computing centers within a minute of collection.

For the EM follow-up program, three independent GW detection algorithms (trigger generators), ran promptly as data became available, generating candidate triggers with latencies between five and eight minutes. Omega Pipeline and coherent WaveBurst (cWB), which are both described in Abadie et al. (2010a), searched for transients (bursts) without assuming a specific waveform morphology. The Multi-Band Template Analysis (MBTA) (Marion 2004), searched for signals from coalescing compact binaries. Triggers were ranked by their "detection statistic", a figure of merit for each analysis, known as Ω, η, and $\rho_{combined}$, respectively. The statistics η for cWB and $\rho_{combined}$ for MBTA are related to the amplitude SNR of the signal across all interferometers while Ω is related to the Bayesian likelihood of a GW signal being present. Triggers with a detection statistic above a nominal threshold, and occurring in times where all three detectors were operating normally, were recorded in the Gravitational-wave Candidate Event Database (GraCEDb).

The trigger generators also produced likelihood maps over the sky (skymaps), indicating the location from which the signal was most likely to have originated. A brief introduction to each trigger generator is presented in Sects. 4.1.1 – 4.1.3.

4.1.1. Coherent WaveBurst

Coherent WaveBurst has been used in previous searches for GW bursts, such as Abbott et al. (2009b) and Abadie et al. (2010a).

The algorithm performs a time-frequency analysis of data in the wavelet domain. It coherently combines data from all detectors to reconstruct the two GW polarization waveforms $h_+(t)$ and $h_\times(t)$ and the source coordinates on the sky. A statistic is constructed from the coherent terms of the maximum likelihood ratio functional (Flanagan & Hughes 1998; Klimenko et al. 2005) for each possible sky location, and is used to rank each location in a grid that covers the sky (skymap). A detailed description of the likelihood analysis, the sky localization statistic and the performance of the cWB algorithm is published elsewhere (Klimenko et al. 2011).

The search was run in two configurations which differ in their assumptions about the GW signal. The "unconstrained" search places minimal assumptions on the GW waveform, while the "linear" search assumes the signal is dominated by a single GW polarization state (Klimenko et al. 2011). While the unconstrained search is more general, and is the configuration that was used in previous burst analyses, the linear search has been shown to better estimate source positions for some classes of signals. For the online analysis, the two searches were run in parallel.

4.1.2. Omega Pipeline

In the Omega Pipeline search (Abadie et al. 2010a), triggers are first identified by performing a matched filter search with a bank of basis waveforms which are approximately (co)sine-Gaussians. The search assumes that a GW signal can be decomposed into a small number of these basis waveforms. Coincidence criteria are then applied, requiring a trigger with consistent frequency in another interferometer within a physically consistent time window. A coherent Bayesian position reconstruction code (Searle et al. 2008, 2009) is then applied to remaining candidates. The code performs Bayesian marginalization over all parameters (time of arrival, amplitude and polarization) other than direction. This results in a skymap providing the probability that a signal arrived at any time, with any amplitude and polarization, as a function of direction. Further marginalization is performed over this entire probability skymap to arrive at a single number, the estimated probability that a signal arrived from any direction. The Ω statistic is constructed from this number and other trigger properties.

4.1.3. MBTA

The Multi-Band Template Analysis (MBTA) is a low-latency implementation of the matched filter search that is typically used to search for compact binary inspirals (Marion 2004; Buskulic 2010). In contrast to burst searches which do not assume any particular waveform morphology, MBTA specifically targets the waveforms expected from NS-NS, NS-BH and BH-BH inspirals. In this way it provides complementary coverage to the burst searches described above.

The search uses templates computed from a second order post-Newtonian approximation for the phase evolution of the signal, with component masses in the range 1–34 $M_\odot$ and a total mass of $< 35 M_\odot$. However, triggers generated from templates with *both* component masses larger than the plausible limit of the NS mass—conservatively taken to be 3.5 $M_\odot$ for this check—were not considered for EM follow-up, since the optical emission is thought to be associated with the merger of two neutron stars or with the disruption of a neutron star by a stellar-mass black hole.

Triggers from each interferometer are clustered and used to search for coincidence among the individual detectors. To generate a candidate event for follow-up, triggers with consistent physical parameters must be present in all three LIGO/Virgo interferometers. For each triple coincident trigger, the sky location was estimated using the time delay between detector sites and the amplitude of the signal measured in each detector (Fairhurst 2009). Before the observing period, a set of simulated gravitational wave signals was used to measure the distribution of errors in recovering the time delays and signal amplitudes. The sky localization algorithm then uses these distributions to assign probabilities to each pixel on the sky.

4.2. Estimating False Alarm Rates

The primary quantity used to decide whether an event should be considered a candidate for follow-ups was its FAR, the average rate at which noise fluctuations create events with an equal or greater value of the detection statistic. For the winter run, a FAR of less than 1 event per day of livetime was required to send an imaging request to the ground-based telescopes, with a higher threshold for Swift. For the autumn run, the FAR threshold was 0.25 events per day of livetime for most telescopes, with stricter requirements for sending triggers to Palomar Transient Factory and Swift. Livetime is here defined as time all three interferometers were simultaneously collecting usable science data.

As in previous all-sky burst searches, e.g. Abbott et al. (2009b) and Abadie et al. (2010a), the FAR for the two burst pipelines was evaluated using the time-shift method. In this method, artificial time shifts, between one second and a few hundred seconds, are applied to the strain series of one or more interferometers, and the shifted data streams are analyzed with the regular coherent search algorithm. The shifted data provide an estimate of the background noise trigger rate without any true coincident gravitational wave signals. During the online analysis, at least 100 time shifts were continuously evaluated with latencies between 10 minutes and several hours. The FAR of each event candidate was evaluated with the most recent available time shifts.

The MBTA pipeline evaluated the FAR analytically based on single interferometer trigger rates, rather than using time shifts. This is computationally simpler than the burst method. It is valid since MBTA is a coincident rather than a coherent analysis, and allows the FAR to be evaluated with data from the minutes immediately preceding the trigger time (Marion 2004).

4.3. Online Data Quality

A number of common occurrences may make a stretch of interferometer data unsuitable for sensitive GW searches. Examples include times of large seismic disturbance, non-standard interferometer configurations, and temporary saturations of various photodiodes in the interferometer sensing and control system. To mark such times, monitor programs analyze auxiliary data to produce lists of abnormal time segments with low latency. When a trigger was identified, it was automatically checked against these lists; triggers which occurred in stretches of unacceptable data were automatically rejected.

4.4. Manual Event Validation

In addition to automated checks on data quality, significant triggers were manually vetted. Trigger alerts were broadcast to collaboration members via e-mail, text message, a website, and in the interferometer control rooms as audio alarms. For each alert, a low-latency pipeline expert conferred with personnel at each of the three observatory sites to validate the event. Pipeline experts and scientists monitoring data on-site provided 24/7 coverage in 8 hour shifts. Assigned personnel confirmed the automated data quality results, checked plots for obvious abnormalities, and verified that there were no known disturbances at any of the three observatory sites.

The intention of manual event validation was to veto spurious events caused by known non-GW mechanisms that have not been caught by low-latency data quality cuts, not to remove every non-GW trigger. In fact, at current sensitivities, most or all of the triggers are unlikely to represent true astrophysical events. The trade-off for this additional check on the quality of the triggers was added latency (usually 10 to 20 minutes) between trigger identification and reporting to the EM observatories. It is possible that as the search matures in the Advanced LIGO/Virgo era the validation process can be fully automated.

5. Choosing Fields to Observe

The uncertainty associated with GW position estimates, expected to be several tens of square degrees (Fairhurst 2009), is large compared to the FOV of most astronomical instruments. Moreover, the likely sky regions calculated from interferometer data may be irregularly shaped, or even contain several disjoint regions. It is impractical to image these entire regions given a limited amount of observing time for a given instrument. There is thus a need to carefully prioritize fields, or tiles, of an instrument to optimize the likelihood of imaging the true gravitational wave source.

The LUMIN software package was created to gather GW triggers from the three trigger generators, and use the skymaps and locations of known galaxies to select fields for each optical or radio instrument to observe. In addition, LUMIN includes tools that were used to facilitate trigger validation (Sect. 4.4) and communication with robotic telescopes. Fields for observation with the Swift XRT and UVOT were selected with slightly different criteria by a separate software package, the Gravitational to Electro-Magnetic Processor (GEM). During the testing process, GEM also applied the tiling criteria for optical telescopes to simulated skymaps, and so provided an important consistency check between LUMIN and GEM.

5.1. Galaxy Catalog

The Gravitational Wave Galaxy Catalog (GWGC) (White et al. 2011) was created to help this and future searches quickly identify nearby galaxies.

The catalog contains up-to-date information compiled from the literature on sky position, distance, blue magnitude, major and minor diameters, position angle and galaxy type for 53,225 galaxies ranging out to 100 Mpc, as well as 150 Milky Way globular clusters. White et al. (2011) compared the catalog with an expected blue light distribution derived from SDSS data and concluded that the GWGC is nearly complete out to ~40 Mpc. The catalog improves on the issue of multiple entries for the same galaxy suffered by previous catalogs by creating the GWGC from a subset of 4 large catalogs, each of which lists a unique Principal Galaxy Catalogue (PGC) number for every galaxy (Paturel et al. 1989). The catalogs used were: an updated version of the Tully Nearby Galaxies Catalog (Tully 1987), the

Catalog of Neighboring Galaxies (Karachentsev et al. 2004), the V8k catalog (Tully et al. 2009), and HyperLEDA (Paturel et al. 2003). Also included is a list of 150 known Milky Way globular clusters (Harris 1996). These are all available freely online, but a local, homogeneous list is essential for rapid follow-up purposes.

5.2. Weighting and Tiling Algorithm

To make use of the galaxy catalog, and choose tiles for each GW trigger, similar algorithms have been implemented in the GEM and LUMIN software packages.

The position information from the trigger generators (see Sect. 4.1) is encoded in skymaps that assign a likelihood to each $0.4° \times 0.4°$ pixel in a grid covering the sky. In practice, only the 1000 most likely pixels are retained, limiting the sky area to roughly 160 square degrees. The search volume is further limited by keeping only objects in the catalog with an estimated distance of less than 50 Mpc, as the current sensitivity of the GW detectors makes it unlikely that binaries containing a neutron star would be detectable beyond this distance. Approximately 8% of the pixels in an average skymap contain a local galaxy or globular cluster listed in the GWGC catalog.

For burst triggers, the tiling algorithms treat the luminosity of each galaxy or globular cluster as a prior for its likelihood to host a GW emitting event. The blue light luminosity is used as a proxy for star formation, indicating the presence of massive stars that may be GW burst progenitors themselves and may evolve into compact binaries that eventually merge. In addition, weak sources of GWs are assumed to be more numerous than strong sources, so that a closer galaxy should contain more *detectable* sources than a more distant galaxy of the same mass (Nuttall & Sutton 2010). This leads to assigning the following likelihood to each pixel:

$$P \propto \sum_i \frac{M_i L}{D_i} \qquad (1)$$

where L is the likelihood based only on the GW data, and M and D are the blue light luminosity (a rough proxy for mass) and distance of the associated galaxy or globular cluster. The sum is over all the objects associated with a particular pixel (which will be 0 or 1 galaxy for the majority of pixels). Extended nearby sources which have a major axis larger than the pixel size have their mass divided evenly over each pixel falling within the ellipse of the disk defined by their major and minor axes. Once this calculation is performed for each pixel, the entire skymap is renormalized to a total likelihood equal to unity.

Unlike the burst algorithms, MBTA assumes the GW source is a merging binary, and estimates some of the source's physical parameters for each trigger. This allows the galaxy catalog to be applied in a slightly different way. Each interferometer measures a quantity known as *effective distance*

$$D_{\text{eff}} = D \left[F_+^2 \left(\frac{1 + \cos^2 \iota}{2} \right)^2 + F_\times^2 \cos^2 \iota \right]^{-1/2}, \qquad (2)$$

where D is the actual distance to the source, ι is the inclination angle between the direction to the observer and the angular momentum vector of the binary, and F_+ and $F_\times$ are the antenna response functions of the particular interferometer. The important feature of the effective distance is that it is always greater than or equal to the true distance to the source. For each MBTA trigger

the galaxy catalog is then only considered out to the smallest effective distance measured for that trigger, with a maximum possible effective distance of 50 Mpc. After the catalog is downselected in this way, each pixel is weighted by the fraction of the catalog's total mass contained in that pixel, i.e.

$$P = \sum_i M_i^{\text{frac}} L, \qquad (3)$$

with the sum over all galaxies associated with the pixel, and $\sum_k M_k^{\text{frac}} = 1$ for a sum over the downselected catalog.

These procedures require a pixel's coordinates to be consistent with a known galaxy's location to be targeted by telescopes. However, in the case that the skymap does not intersect with any galaxies in the catalog, the likelihood from the GW skymap alone is used as each pixel's likelihood ($P = L$). In practice, this is a very rare occurrence and only happens in the case of a very well-localized skymap.

The actual pointing coordinates requested for each telescope are selected to maximize the total contained P summed over pixels within the FOV. If multiple pointings are allowed with the same instrument, additional tiles with the next highest ranking are then selected. The tile selection process is illustrated in Fig. 3.

5.3. Galaxy Targeting for Small-Field Instruments

The logic used for selecting pointings for the Swift satellite was similar to that of ground-based telescopes, except that, because the narrower Swift FOV required greater precision, care was taken to ensure the target galaxies were within the selected field. The coordinates supplied to Swift for follow-up were those of the matched galaxy itself in cases where there was only a single galaxy in a pixel, but the center of the $0.4° \times 0.4°$ pixel in cases where the central coordinates of an extended source were outside the pixel or there were multiple galaxies in the pixel. Since fewer follow-ups were allowed using Swift than with other scopes, a minimum requirement was placed on the statistic P contained within the pixels selected for X-ray observation.

Zadko and Liverpool Telescope also have relatively narrow fields. For these telescopes, no attempt was made to capture multiple galaxies in a single field. Instead, the weighting scheme in Eqn. 1 was applied to each galaxy rather than each pixel, and the center coordinates of the top ranked galaxies were passed to the observatories.

6. Performance Study

6.1. Simulated Waveform Injections

An ensemble of simulated GW signals was generated to measure the effectiveness of the reconstruction and follow-up procedures. For the Omega and cWB burst pipelines, these "software injections" were a mix of ad hoc sine-Gaussian, Gaussian, and white noise burst waveforms similar in type and distribution to those used in previous LIGO/Virgo all-sky analyses (Abbott et al. 2009b; Abadie et al. 2010a). While these waveforms are not based on specific astrophysical models, they do a good job of characterizing detector response for signals in specific frequency ranges (sine-Gaussians) and broadband signals (white-noise bursts). For MBTA (see Sect. 4.1.3), injections were drawn from NS-NS and NS-BH inspiral waveforms with a range of parameters. To emulate a realistic spatial distribution, each injection was calculated with a source distance and
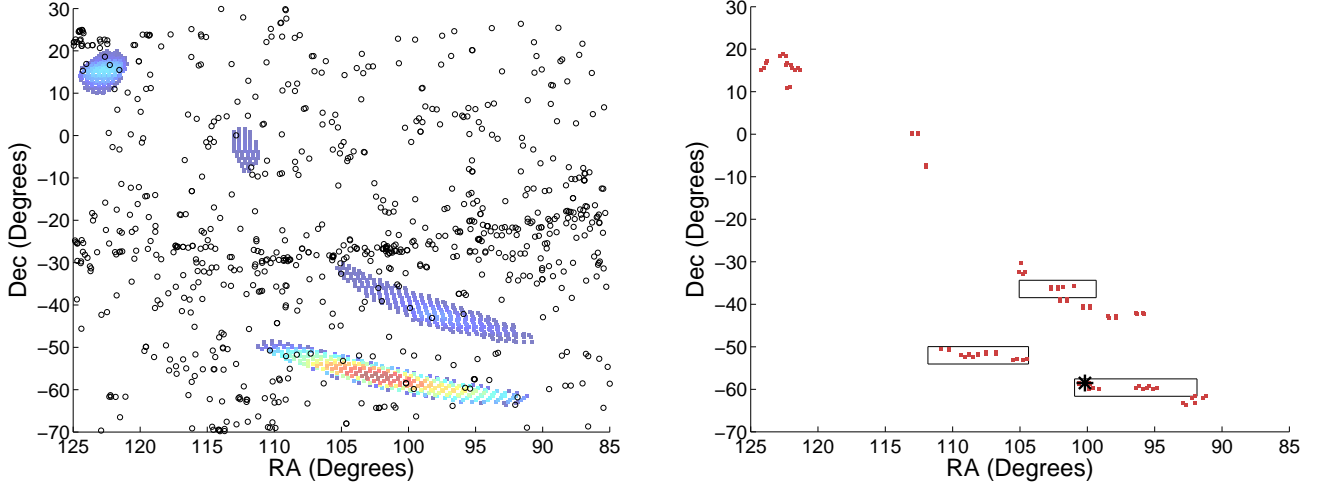
Fig. 3. The weighting and tiling process for a simulated signal reconstructed by cWB. The skymap is shown in the left panel with the highest likelihood regions in red, and lower ranked pixels in blue, along with galaxy locations marked as black circles. The right panel shows the location and approximate size of the three chosen QUEST tiles, along with the locations of pixels that are retained after weighting by the galaxy catalog. The injection location is caught by the southernmost tile, and is marked with an asterisk.
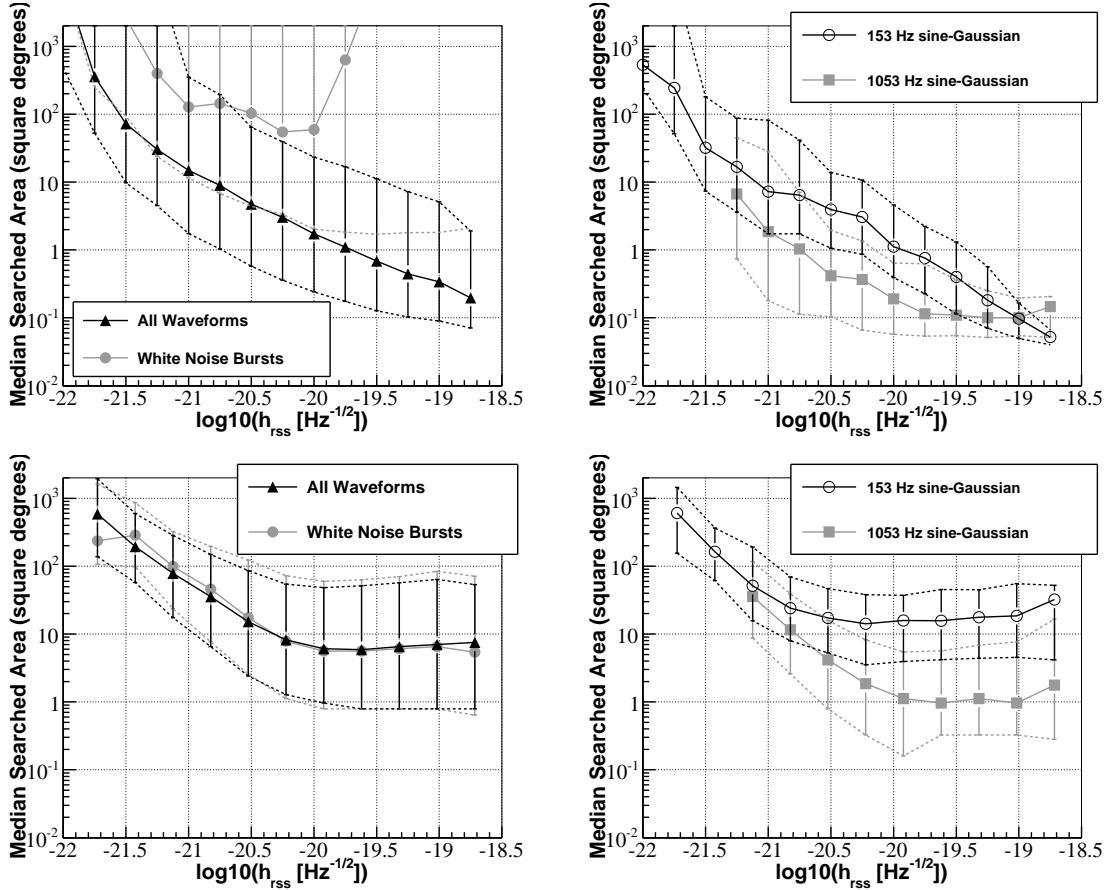
Fig. 4. Plots of typical uncertainty region sizes for the Omega (top) and unconstrained cWB (bottom) pipelines, as a function of GW strain amplitude at Earth, for various waveform types. The "searched area" is the area of the skymap with a likelihood value greater than the likelihood value at the true source location *before* the galaxy catalog is used to further limit the search region. The solid line with symbols represents the median (50%) performance, while the upper and lower dashed lines show the 75% and 25% quartile values. Near the detection threshold ($h_{rss} \sim 10^{-21}$ Hz$^{-1/2}$) , uncertainty regions are typically between 10 and 100 square degrees. The Omega pipeline performs poorly on white noise bursts but exceptionally well on sine-Gaussians because it is designed to identify signals that are well-localized in frequency space.

direction inside a randomly selected galaxy from the GWGC and the simulated GW amplitudes were weighted to be inversely proportional to distance. Only galaxies within 50 Mpc were included in the simulation, with weighting factors applied so that the probability of originating from each galaxy was proportional to its blue light luminosity. The simulation set and the analysis used the same catalog, so the results presented in Figures 6 – 8 make the assumption that the blue light luminosity distribution of galaxies in the GWGC is a good tracer of GW sources in the local universe. Signals were superimposed on real LIGO-Virgo gravitational wave data taken between August and December 2009.

While performance studies in this paper were done using software injections, a relatively small number of tests in which a signal was physically put into the interferometer via actuators ("hardware injections") were also performed, providing an additional cross-check.

6.2. Testing Results

Because the skymap likelihood regions are often irregularly shaped, the size of the uncertainty region is characterized by the "searched area", defined as the angular area of the skymap with likelihood greater than the likelihood at the true source location. The median searched area as a function of signal strength is plotted for both cWB and Omega Pipeline in Fig. 4. Here, gravitational wave amplitudes are expressed in terms of their root-sum-squared amplitude:

$$h_{\mathrm{rss}} \equiv \sqrt{\int \left(|h_+(t)|^2 + |h_\times(t)|^2 \right) \mathrm{d}t} \qquad (4)$$

where $h_+(t)$ and $h_\times(t)$ are the plus- and cross-polarization strain functions of the wave. Since h is a dimensionless quantity, h_{rss} is given in units of $\mathrm{Hz}^{-1/2}$. For this data, signals near the detection threshold would have $h_{\mathrm{rss}} \sim 10^{-21}\,\mathrm{Hz}^{-1/2}$, roughly corresponding to the cWB statistic $\eta \sim 5$ (Abadie et al. 2010a). These signals were typically localized with median search areas of several tens of square degrees. The coherent position reconstruction algorithms are "tuned" to localize these near-threshold signals as accurately as possible; as a result, some of the plots reveal a degradation in algorithm performance for very loud signals. Median searched area is shown for MBTA in Fig. 5, as a function of the combined SNR of the signal:

$$\rho_{\mathrm{combined}} \equiv \sqrt{\rho_{\mathrm{H1}}^2 + \rho_{\mathrm{L1}}^2 + \rho_{\mathrm{V1}}^2}, \qquad (5)$$

where ρ_{H1}^2, ρ_{L1}^2, and ρ_{V1}^2 are the single detector SNRs seen in the Hanford, Livingston and Virgo instruments, respectively.

The simulated GW signals described above were also used to test the tiling software in order to determine the success rate for imaging the correct sky location with realistic detector noise, reconstructed skymap shapes, and telescope FOVs. The LUMIN software package was used to determine pointings for ground-based telescopes and GEM was used for Swift.

Some of the results of this simulation can be seen in Fig. 6. The results are plotted as a function of the ranking statistic used by each pipeline. On the y-axis, the "Fraction of triggers imaged" represents the fraction of triggers with the given detection statistic that have the correct image location included within the selected tiles. Given a GW trigger, the success rate plotted in Fig. 6 estimates the odds of choosing the right sky position. In this figure, note that the "whole skymap" is limited to 160
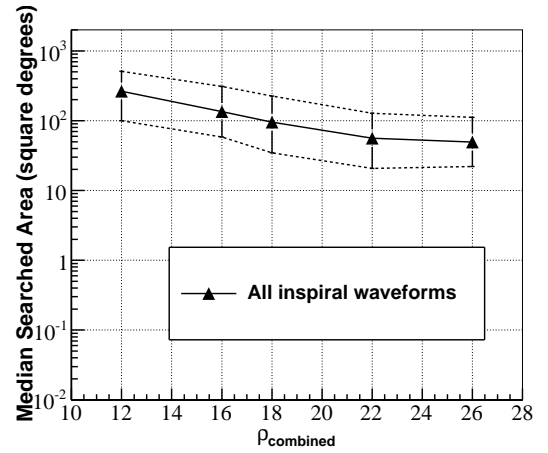

Fig. 5. Plots of uncertainty region sizes for the MBTA pipeline as a function of combined SNR (ρ_{combined}). The solid line with symbols represents the median (50%) performance, while the upper and lower dashed lines show the 75% and 25% quartile values. The expected detection threshold is around $\rho_{\mathrm{combined}} \sim 12$.

square degrees, and so does not always include the true source location. The thresholds for initiating follow-ups varied with the condition of the interferometers, but was typically around 3.0 for Ω, $\eta = 3.5$ for cWB, and $\rho_{\mathrm{combined}} = 10$ for MBTA. The complex behavior of the Omega efficiency curve is related to the use of a hybrid detection statistic which utilizes different methods depending on SNR range. Clearly, events with SNR near the threshold for triggering follow-ups, the most likely scenario for the first detections, are the most difficult to localize.

Example efficiency curves for the burst simulation are shown in Fig. 7. The efficiency for each marker on the plot is calculated as the fraction of signals for which the injected location was successfully imaged, for an h_{rss} range centered on the marker. Specifically, we require that:

1. The trigger's ranking statistic is higher than the threshold, which is chosen to enforce a FAR of about 1 GW trigger per day of livetime.
2. The true source location is included in one of the chosen tiles. Five tiles are allowed for Swift, three tiles for the QUEST camera, and one tile for all other telescopes.

Note that efficiencies in this figure do not reach unity even for loud events primarily due to the difficulty of correctly localizing GWs in some regions of the sky where the antenna response of one or more interferometers is poor.

The efficiencies produced with these criteria are upper limits on what would be detected in a real search. They assume that the EM transient is very bright, and will always be detected if the correct sky location is imaged. The quoted efficiencies do not account for the fact that some chosen tiles will not be observed due to restrictions from weather, instrument availability, proximity to the Sun or Moon, or the application of a manual veto. The exact behavior of the efficiency curves will vary depending on the morphologies of the simulation waveforms selected. Finally, the chosen GW trigger FAR of one event per day presumes the false alarm fraction from the EM transient classification pipeline will be low enough to make a coincidence significant.

Nevertheless, these curves provide a measure of the potential for joint EM/GW searches. If the number of incidental EM tran-
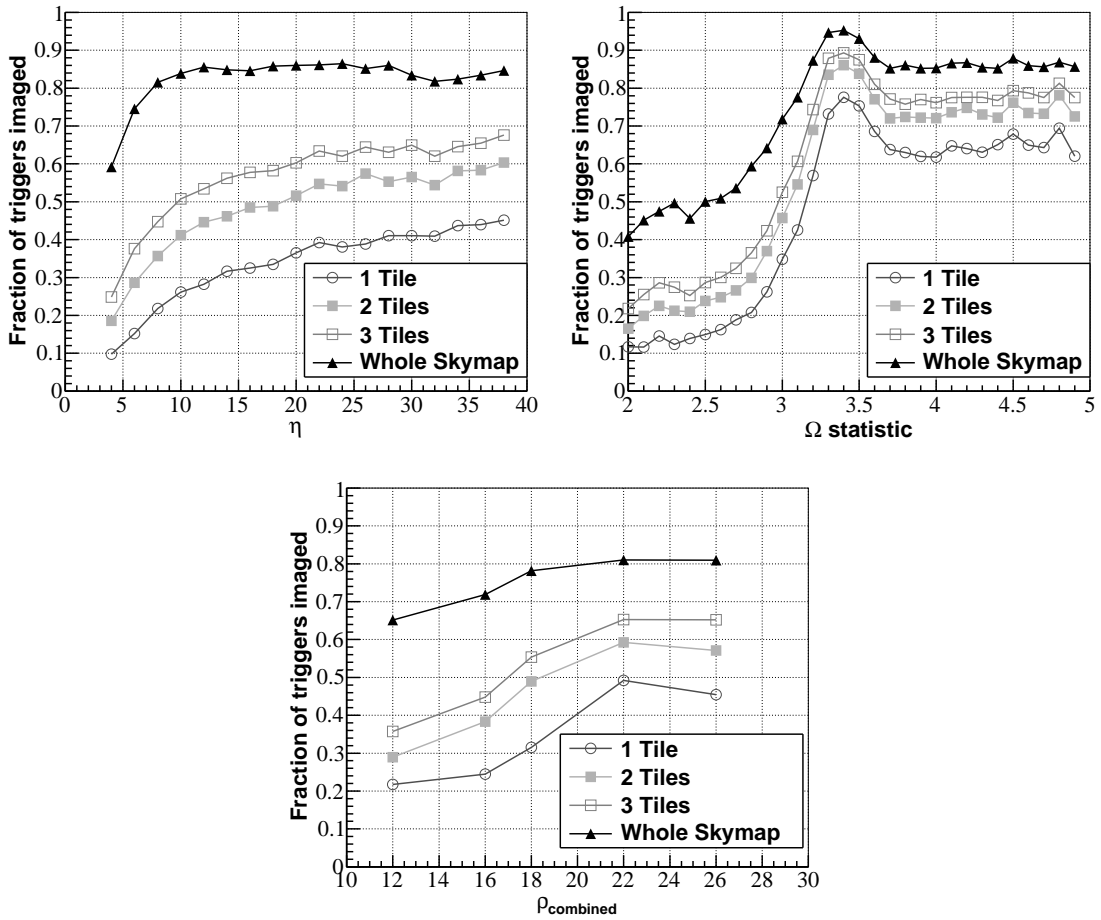
Fig. 6. Success rates for the tile selection process based on unconstrained cWB (left), Omega (right), and MBTA (bottom) skymaps. An injection recovered with the detection statistic shown on the horizontal axis is considered a success if the correct source location is included in one of the chosen tiles. Typical thresholds for follow-up are Ω=3.0, η=3.5, and ρ_{combined}=10. Each tile is $1.85° \times 1.85°$, the FOV of both the ROTSE and TAROT telescopes. Statistical uncertainties are small with respect to the markers.

sients in the observed fields can be understood and controlled, then the addition of EM data can effectively increase the search sensitivity to very weak GW signals. For occasional strong GW signals, the plots suggest that only a few pointings of a telescope are enough to image the true location with better than 50% efficiency.

6.3. Calibration Uncertainty

Uncertainty in the calibration of GW detectors may impact the ability to correctly choose the right fields to observe with EM instruments. To estimate the potential detriment to pointing, we generated a second set of simulated burst signals, with each signal including some level of miscalibration corresponding to realistic calibration errors. Before being added to detector noise, each astrophysical signal was scaled in amplitude by a factor between 0.85 and 1.15, and shifted in time by between −150 and 150 μs. The exact amplitude and time "jitter" were randomly selected from flat distributions for each signal entering each detector. The bounds of the distribution of values for the timing and amplitude jitter were chosen to match preliminary estimates for the LIGO and Virgo calibration error budgets around 150 Hz for the 2009–2010 run. Well above this frequency, the actual timing

errors are likely less than this model; the simulation is conservative in this sense.

Some of the results of this simulation, with the cWB algorithm, may be seen in Fig. 8. The success rate is shown for the entire pipeline, assuming one pointing of a $1.85° \times 1.85°$ FOV, three pointings of the QUEST FOV, and five pointings of a Swift FOV. The curves are shown both with and without the effects of calibration uncertainty. For the low SNR signals that are the most likely for first detections, $\eta \lesssim 10$, the efficiency is within a few percent with and without the calibration uncertainty. This is expected, since at low signal to noise ratio, timing uncertainty from detector noise is larger than timing uncertainty due to calibration (Fairhurst 2009). However, for louder signals, the ability to correctly choose the right sky location is seen to be modestly impacted by the accuracy of the calibration.

7. Summary

Mergers of compact binary systems containing neutron stars, as well as some other energetic astrophysical events, are expected to emit observable transients in both the gravitational wave and electromagnetic channels. Observing populations of joint signals would likely reveal many details of the GW sources, and could even constrain cosmological models.
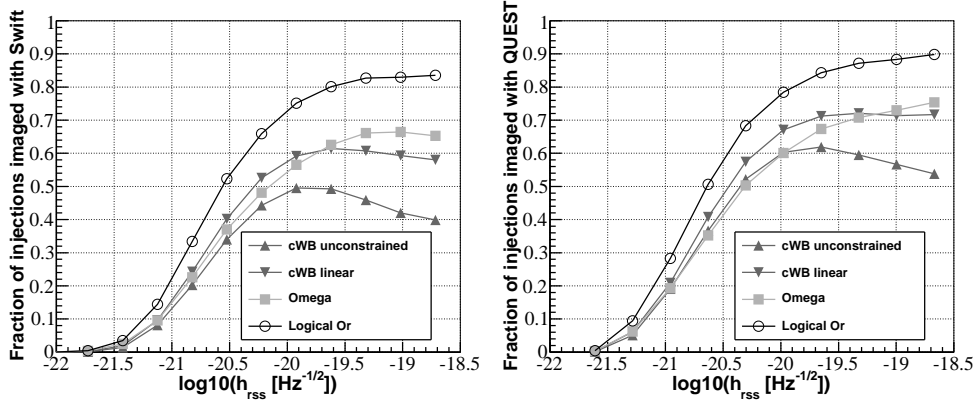
Fig. 7. Fractional success as a function of strain at Earth for combinations of the Omega and cWB burst pipelines. Success rates assume 5 pointings for each event for Swift (left) and 3 for QUEST (right). Fractional success is end-to-end from triggering by pipeline to successful pointing, with a threshold for follow-up approximating a FAR of one per day. The "Logical Or" curve counts a success if either linear cWB or Omega correctly localized the event, effectively doubling the allowed number of tiles. Some curves show degraded performance for very loud signals because the algorithms are tuned to optimize performance for weaker events close to the detection threshold. Statistical uncertainties are small with respect to the markers.
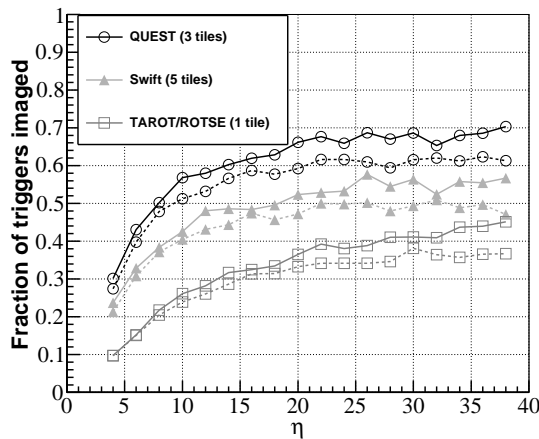
Fig. 8. Fractional success rate for simulated gravitational wave signals with (dashed) and without (solid) including calibration uncertainties. QUEST results assume 3 pointings, Swift results assume 5 pointings and TAROT/ROTSE results assume 1 pointing.

During 2009 and 2010, the LIGO and Virgo collaborations partnered with a large, heterogeneous group of EM observatories to jointly seek transient signals. X-ray, optical, and radio observatories collected follow-up observations to GW triggers that were delivered with ~30 minutes of latency. Analysis of the multi-instrument data set is currently in progress, and the results of the search for jointly observed transients will be published at a later date.

A Monte Carlo study of the GW data analysis algorithms used in the low latency pipeline demonstrated the ability of the LIGO/Virgo network to localize transient GW events on the sky. Localization ability depends strongly on the SNR of the GW signal; lower SNR signals are more difficult to localize, but are also the more likely scenario for the first detections. Signals with SNR near the detection threshold were localized with median sky areas between 10 and 100 square degrees. After limiting the search to known galaxies and Milky Way globular clusters within the detection range of the GW observatories, the simulation shows that the correct location of signals detected near

threshold can be imaged with 30-50% success with three fields of size $1.85° \times 1.85°$, for instance. Moreover, the ability to image the source position is seen to be only marginally impacted by realistic levels of calibration uncertainty.

This search establishes a baseline for low-latency analysis with the next-generation GW detectors Advanced LIGO and Advanced Virgo. Installation of these second-generation detectors is already in progress, with observations expected to begin around 2015. Developing a low-latency response to GW triggers represents the first steps toward solving the many logistical and technical challenges that must be overcome to collect prompt, multiwavelength, EM observations of GW source progenitors. The integration of GW and EM observatories is likely to continue to develop over the next few years as the scientific community prepares to utilize the many opportunities promised by the impending global network of advanced GW detectors.

References

Abadie, J. et al. 2010a, Phys. Rev. D, 81, 102001

Abadie, J. et al. 2010b, Classical and Quantum Gravity, 27, 173001

Abbott, B. P. et al. 2009a, Reports on Progress in Physics, 72, 076901

Abbott, B. P. et al. 2009b, Phys. Rev. D, 80, 102001

Abbott, B. P. et al. 2010, ApJ, 715, 1438

Accadia, T., Acernese, F., Antonucci, F., et al. 2011, Classical and Quantum Gravity, 28, 114002

Acernese, F. et al. 2008, Classical and Quantum Gravity, 25, 184001

Akerlof, C. W., Kehoe, R. L., McKay, T. A., et al. 2003, PASP, 115, 132

Andersson, N., Ferrari, V., Jones, D. I., et al. 2011, General Relativity and Gravitation, 43, 409

Baltay, C., Rabinowitz, D., Andrews, P., et al. 2007, PASP, 119, 1278

Beacom, J. F. & Vogel, P. 1999, Phys. Rev. D, 60, 033007

Berger, E. 2010, ApJ, 722, 1946

Bloom, J. S. et al. 2009, Preprint, arXiv:0902.1527v1

Buskulic, D. 2010, Classical and Quantum Gravity, 27, 194013

Corsi, A. & Mészáros, P. 2009, ApJ, 702

Coward, D. M., Gendre, B., Sutton, P. J., et al. 2011, MNRAS, 415, L26

Coward, D. M., Todd, M., Vaalsta, T. P., et al. 2010, Publications of the Astronomical Society of Australia, 27, 331

Cutler, C., Apostolatos, T. A., Bildsten, L., et al. 1993, Phys. Rev. Lett., 70, 2984

Dalal, N., Holz, D. E., Hughes, S., & Jain, B. 2006, Phys. Rev. D, 74, 063006

Damour, T. & Vilenkin, A. 2000, Phys. Rev. Lett., 85, 3761

de Vos, M., Gunst, A. W., & Nijboer, R. 2009, IEEE Proceedings, 97, 1431

Fairhurst, S. 2009, New Journal of Physics, 11, 123006

Fairhurst, S. 2011, Classical and Quantum Gravity, 28, 105021

Fender, R., Wijers, R., Stappers, B., et al. 2006, Proceedings of Science, MQW6, 104

Flanagan, E. & Hughes, S. 1998, Phys. Rev. D, 57, 4566

Flanagan, E. E. & Hinderer, T. 2008, Phys. Rev. D, 77, 021502

Fryer, C. L., Holz, D. E., & Hughes, S. A. 2002, ApJ, 565, 430

Gehrels, N., Ramirez-Ruiz, E., & Fox, D. B. 2009, ARA&A, 47, 567

Gehrels, N. et al. 2004, ApJ, 611, 1005

Granot, J., Panaitescu, A., Kumar, P., & Woosley, S. E. 2002, ApJ, 570, L61

Halzen, F. & Raffelt, G. G. 2009, Phys. Rev. D, 80, 087301

Harris, W. E. 1996, AJ, 122, 1487

Harry, G. M. et al. 2010, Classical and Quantum Gravity, 27, 084006

Hinderer, T., Lackey, B. D., Lang, R. N., & Read, J. S. 2010, Phys. Rev. D, 81, 123016

Kahya, E. K. 2011, Phys. Lett. B, 701, 291

Kann, D. A., Klose, S., Zhang, B., et al. 2011, ApJ, 734, 96

Kann, D. A., Klose, S., Zhang, B., et al. 2010, ApJ, 720, 1513

Kanner, J., Huard, T. L., Marka, S., et al. 2008, Classical and Quantum Gravity, 25, 184034

Karachentsev, I. D., Karachentseva, V. E., Huchtmeie, W. K., & Makarov, D. I. 2004, AJ, 127, 2031

Keller, S. C., Schmidt, B. P., Bessell, M. S., et al. 2007, Publications of the Astronomical Society of Australia, 24(1), 1

Kelley, L. Z., Ramirez-Ruiz, E., Zemp, M., Diemand, J., & Mandel, I. 2010, ApJL, 725, L91

Kiuchi, K., Shibata, M., Montero, P. J., & Font, J. A. 2011, Physical Review Letters, 106, 251102

Klimenko, S., Mohanty, S., Rakhmanov, M., & Mitselmakher, G. 2005, Phys. Rev. D, 72, 122002

Klimenko, S., Vedovato, G., Drago, M., et al. 2011, submitted to Phys. Rev. D

Klotz, A., Boer, M., Atteia, J. L., & Gendre, B. 2009a, AJ, 137, 4100

Klotz, A., Gendre, B., Atteia, J. L., et al. 2009b, ApJL, 697, L18

Kobayashi, S. & Mészáros, P. 2003a, ApJ, 589, 861

Kobayashi, S. & Mészáros, P. 2003b, Astrophys. J., 585, L89

Kochanek, C. S. & Piran, T. 1993, ApJL, 417, L17

Korobkin, O., Abdikamalov, E. B., Schnetter, E., Stergioulas, N., & Zink, B. 2011, Phys. Rev. D, 83, 043007

Kulkarni, S. R. & Kasliwal, M. M. 2009, Preprint, arXiv:0903.0218

Kuroda, K. & The LCGT Collaboration. 2010, Classical and Quantum Gravity, 27, 084004

Law, N. M., Kulkarni, S. R., Dekany, R. G., et al. 2009, PASP, 121, 1395

Leonor, I., Cadonati, L., Coccia, E., et al. 2010, Classical and Quantum Gravity, 27, 084019

Li, L. & Paczyński, B. 1998, ApJ, 507, L59

Lück, H. et al. 2010, J. Phys. Conf. Ser., 228, 012012

MacFadyen, A. I. & Woosley, S. E. 1999, ApJ, 524, 262

Malek, K., Batsch, T., Cwiok, M., et al. 2009, Proceedings of SPIE, 7502, 75020D

Marion, F. 2004, Proceedings of Rencontres de Moriond on Gravitational Waves and Experimental Gravity 2003

Markovic, D. 1993, Phys. Rev. D, 48, 4738

Mészáros, P. 2006, Reports on Progress in Physics, 69, 2259

Metzger, B. D., Giannios, D., Thompson, T. A., Bucciantini, N., & Quataert, E. 2011, MNRAS, 413, 2031

Metzger, B. D., Martinez-Pinedo, G., Darbha, S., et al. 2010, MNRAS, 406, 2650

Nakar, E. 2007, Physics Reports, 442, 166

Nissanke, S., Holz, D. E., Hughes, S. A., Dalal, N., & Sievers, J. L. 2010, ApJ, 725, 496

Nuttall, L. K. & Sutton, P. J. 2010, Phys. Rev. D, 82, 102002

O'Leary, R. M., O'Shaughnessy, R., & Rasio, F. A. 2007, Phys. Rev. D, 76, 061504

Ott, C. D. 2009, Classical and Quantum Gravity, 26, 063001

Pannarale, F., Rezzolla, L., Ohme, F., & Read, J. S. 2011, Preprint, arXiv:1103.3526

Paturel, G., Fouque, P., Bottinelli, L., & Gouguenheim, L. 1989, AAS, 80, 299

Paturel, G., Petit, C., Prugniel, P., et al. 2003, A&A, 412, 45

Perley, R. A., Chandler, C. J., Butler, B. J., & Wrobel, J. M. 2011, Preprint, arXiv:1106.0532

Piran, T. 2004, Reviews of Modern Physics, 76, 1143

Piro, A. L. & Pfahl, E. 2007, ApJ, 658, 1173

Rau, A., Kulkarni, S. R., Law, N. M., et al. 2009, PASP, 121, 1334

Rhoads, J. E. 2003, ApJ, 591, 1097

Rykoff, E. S., Aharonian, F., Akerlof, C. W., et al. 2005, ApJ, 631, 1032

Schutz, B. F. 1986, Nature, 323, 310

Schutz, B. F. 2011, Classical and Quantum Gravity, 28, 125023

Searle, A. C., Sutton, P. J., & Tinto, M. 2009, Classical and Quantum Gravity, 26, 155017

Searle, A. C., Sutton, P. J., Tinto, M., & Woan, G. 2008, Classical and Quantum Gravity, 25, 114038

Seto, N. 2007, Phys. Rev. D, 75, 024016

Siemens, X., Creighton, J., Maor, I., et al. 2006, Phys. Rev. D, 73, 105001

Soderberg, A. M. et al. 2008, Nature, 453, 469

Stappers, B. W., Hessels, J. W. T., Alexov, A., et al. 2011, A&A, 530, A80+

Steele, I. A., Smith, R. J., Rees, P. C., et al. 2004, Proceedings of SPIE, 5489, 679

Stubbs, C. W. 2008, Classical and Quantum Gravity, 25, 184033

Sylvestre, J. 2003, ApJ, 591, 1152

Tully, R. B. 1987, ApJ, 321, 280

Tully, R. B., Rizzi, L., Shaya, E. J., et al. 2009, AJ, 138, 323

Vachaspati, T. 2008, Phys. Rev. Lett., 101, 141301

Vallisneri, M. 2000, Phys. Rev. Lett., 84, 3519

White, D. J., Daw, E. J., & Dhillon, V. S. 2011, Classical and Quantum Gravity, 28, 085016

Will, C. M. 2005, Living Rev. Rel., 9, 3

Woosley, S. E. 1993, ApJ, 405, 273

Woosley, S. E. & Bloom, J. S. 2006, ARA&A, 44, 507

Yunes, N., O'Shaughnessy, R., Owen, B. J., & Alexander, S. 2010, Phys. Rev. D, 82, 064017

1 LIGO - California Institute of Technology, Pasadena, CA 91125, USA

2 California State University Fullerton, Fullerton CA 92831 USA

3 SUPA, University of Glasgow, Glasgow, G12 8QQ, UK

4 Laboratoire d'Annecy-le-Vieux de Physique des Particules (LAPP), Université de Savoie, CNRS/IN2P3, F-74941 Annecy-Le-Vieux, France

5 INFN, Sezione di Napoli [a]; Università di Napoli 'Federico II'[b] Complesso Universitario di Monte S.Angelo, I-80126 Napoli; Università di Salerno, Fisciano, I-84084 Salerno[c], Italy

6 LIGO - Livingston Observatory, Livingston, LA 70754, USA

7 Albert-Einstein-Institut, Max-Planck-Institut für Gravitationsphysik, D-30167 Hannover, Germany

8 Leibniz Universität Hannover, D-30167 Hannover, Germany

9 University of Wisconsin–Milwaukee, Milwaukee, WI 53201, USA

10 Stanford University, Stanford, CA 94305, USA

11 University of Florida, Gainesville, FL 32611, USA

12 Louisiana State University, Baton Rouge, LA 70803, USA

13 University of Birmingham, Birmingham, B15 2TT, UK

14 INFN, Sezione di Roma[a]; Università 'La Sapienza'[b], I-00185 Roma, Italy

15 LIGO - Hanford Observatory, Richland, WA 99352, USA

16 Albert-Einstein-Institut, Max-Planck-Institut für Gravitationsphysik, D-14476 Golm, Germany

17 Montana State University, Bozeman, MT 59717, USA

18 European Gravitational Observatory (EGO), I-56021 Cascina (PI), Italy

19 Syracuse University, Syracuse, NY 13244, USA

20 University of Western Australia, Crawley, WA 6009, Australia

21 LIGO - Massachusetts Institute of Technology, Cambridge, MA 02139, USA

22 Laboratoire AstroParticule et Cosmologie (APC) Université Paris Diderot, CNRS: IN2P3, CEA: DSM/IRFU, Observatoire de Paris, 10 rue A.Domon et L.Duquet, 75013 Paris - France

23 Columbia University, New York, NY 10027, USA

24 INFN, Sezione di Pisa[a]; Università di Pisa[b]; I-56127 Pisa; Università di Siena, I-53100 Siena[c], Italy

25 Nikhef, Science Park, Amsterdam, the Netherlands[a]; VU University Amsterdam, De Boelelaan 1081, 1081 HV Amsterdam, the Netherlands[b]

26 The University of Texas at Brownsville and Texas Southmost College, Brownsville, TX 78520, USA

27 San Jose State University, San Jose, CA 95192, USA

28 Moscow State University, Moscow, 119992, Russia

29 LAL, Université Paris-Sud, IN2P3/CNRS, F-91898 Orsay[a]; ESPCI, CNRS, F-75005 Paris[b], France

30 NASA/Goddard Space Flight Center, Greenbelt, MD 20771, USA

31 The Pennsylvania State University, University Park, PA 16802, USA

32 Université Nice-Sophia-Antipolis, CNRS, Observatoire de la Côte d'Azur, F-06304 Nice[a]; Institut de Physique de Rennes, CNRS, Université de Rennes 1, 35042 Rennes[b], France

33 Laboratoire des Matériaux Avancés (LMA), IN2P3/CNRS, F-69622 Villeurbanne, Lyon, France

34 Washington State University, Pullman, WA 99164, USA

35 INFN, Sezione di Perugia[a]; Università di Perugia[b], I-06123 Perugia,Italy

36 INFN, Sezione di Firenze, I-50019 Sesto Fiorentino[a]; Università degli Studi di Urbino 'Carlo Bo', I-61029 Urbino[b], Italy

37 University of Oregon, Eugene, OR 97403, USA

38 Laboratoire Kastler Brossel, ENS, CNRS, UPMC, Université Pierre et Marie Curie, 4 Place Jussieu, F-75005 Paris, France

39 Rutherford Appleton Laboratory, HSIC, Chilton, Didcot, Oxon OX11 0QX, UK

40 IM-PAN 00-956 Warsaw[a]; Astronomical Observatory Warsaw University 00-478 Warsaw[b]; CAMK-PAN 00-716 Warsaw[c]; Białystok University 15-424 Białystok[d]; IPJ 05-400 Świerk-Otwock[e]; Institute of Astronomy 65-265 Zielona Góra[f], Poland

41 University of Maryland, College Park, MD 20742 USA

42 University of Massachusetts - Amherst, Amherst, MA 01003, USA

43 The University of Mississippi, University, MS 38677, USA

44 Canadian Institute for Theoretical Astrophysics, University of Toronto, Toronto, Ontario, M5S 3H8, Canada

45 Tsinghua University, Beijing 100084 China

46 University of Michigan, Ann Arbor, MI 48109, USA

47 Charles Sturt University, Wagga Wagga, NSW 2678, Australia

48 Caltech-CaRT, Pasadena, CA 91125, USA

49 INFN, Sezione di Genova; I-16146 Genova, Italy

50 Pusan National University, Busan 609-735, Korea

51 Carleton College, Northfield, MN 55057, USA

52 Australian National University, Canberra, ACT 0200, Australia

53 The University of Melbourne, Parkville, VIC 3010, Australia

54 Cardiff University, Cardiff, CF24 3AA, UK

55 INFN, Sezione di Roma Tor Vergata[a]; Università di Roma Tor Vergata, I-00133 Roma[b]; Università dell'Aquila, I-67100 L'Aquila[c], Italy

56 University of Salerno, I-84084 Fisciano (Salerno), Italy and INFN (Sezione di Napoli), Italy

57 The University of Sheffield, Sheffield S10 2TN, UK

58 RMKI, H-1121 Budapest, Konkoly Thege Miklós út 29-33, Hungary

59 INFN, Gruppo Collegato di Trento[a] and Università di Trento[b], I-38050 Povo, Trento, Italy; INFN, Sezione di Padova[c] and Università di Padova[d], I-35131 Padova, Italy

60 Inter-University Centre for Astronomy and Astrophysics, Pune - 411007, India

61 University of Minnesota, Minneapolis, MN 55455, USA

62 California Institute of Technology, Pasadena, CA 91125, USA

63 Northwestern University, Evanston, IL 60208, USA

64 The University of Texas at Austin, Austin, TX 78712, USA

65 Eötvös Loránd University, Budapest, 1117 Hungary

66 University of Adelaide, Adelaide, SA 5005, Australia

67 University of Szeged, 6720 Szeged, Dóm tér 9, Hungary

68 Embry-Riddle Aeronautical University, Prescott, AZ 86301 USA

69 National Institute for Mathematical Sciences, Daejeon 305-390, Korea

70 Perimeter Institute for Theoretical Physics, Ontario, Canada, N2L 2Y5

71 National Astronomical Observatory of Japan, Tokyo 181-8588, Japan

72 Universitat de les Illes Balears, E-07122 Palma de Mallorca, Spain

73 Korea Institute of Science and Technology Information, Daejeon 305-806, Korea

74 University of Southampton, Southampton, SO17 1BJ, UK

75 Institute of Applied Physics, Nizhny Novgorod, 603950, Russia

76 Lund Observatory, Box 43, SE-221 00, Lund, Sweden

77 Hanyang University, Seoul 133-791, Korea

78 Seoul National University, Seoul 151-742, Korea

79 University of Strathclyde, Glasgow, G1 1XQ, UK

80 Southern University and A&M College, Baton Rouge, LA 70813

81 University of Rochester, Rochester, NY 14627, USA

82 Rochester Institute of Technology, Rochester, NY 14623, USA

83 Hobart and William Smith Colleges, Geneva, NY 14456, USA

84 University of Sannio at Benevento, I-82100 Benevento, Italy and INFN (Sezione di Napoli), Italy

85 Louisiana Tech University, Ruston, LA 71272, USA

86 McNeese State University, Lake Charles, LA 70609 USA

87 University of Washington, Seattle, WA, 98195-4290, USA

88 Andrews University, Berrien Springs, MI 49104 USA

89 Trinity University, San Antonio, TX 78212, USA

90 Southeastern Louisiana University, Hammond, LA 70402, USA

91 "Pi of the Sky" and the Andrzej Soltan Institute for Nuclear Studies, Hoza 69, 00-681 Warsaw, Poland

92 Research School of Astronomy & Astrophysics, Mount Stromlo Observatory, Cotter Road, Weston Creek, ACT 2611, Australia

93 Observatoire de Haute Provence, CNRS, FR 04870 St-Michel l'Observatoire, France

94 Centre d'Etude Spatial des Rayonnements (CESR), 9 Avenue du colonel Roche, 31028 TOULOUSE Cedex 4, France

95 NASA Einstein Fellow

96 Jodrell Bank Center for Astrophysics, University of Manchester, Manchester M13 9PL, UK

97 Liverpool John Moores University, Liverpool L3 2AJ, UK

98 Astronomical Institute "Anton Pannekoek", University of Amsterdam, 1090 GE Amsterdam, The Netherlands